

## RESEARCH ARTICLE

View Article Online  
View Journal | View IssueCite this: *Mater. Chem. Front.*,  
2020, 4, 1158MOF derived high-density atomic platinum  
heterogeneous catalyst for C–H bond activation†Zewen Zhuang,<sup>†</sup> Yu Wang,<sup>‡</sup> Zheng Chen,<sup>‡</sup> Dingsheng Wang,<sup>†</sup>  
Chen Chen,<sup>\*</sup> Qing Peng<sup>\*a</sup> and Yadong Li<sup>†\*</sup>

Densely populated metal atomic site catalysts play a key role in practical catalysis applications. Herein, we report an amorphous nanobox with high-density atomic platinum species which are uniformly dispersed into the ZIF-8 skeleton through cation exchange. During the dispersing process, the ZIF-8 core was gradually etched into the hollow structure though the Kirkendall effect, and a great amount substitutions of Pt with Zn breaks the initial long-range ordered ZIF-8 topology into a distorted skeleton which leads to the significantly unsaturated coordination of atomic Pt species. The high-density atomic Pt nanoboxes exhibit excellent performance in direct C–H bond borylation of arenes which are usually catalyzed by homogeneous complexes. Such high-density atomic site heterogeneous catalysts could serve as a bridge to convert from homogeneous to heterogeneous catalysis.

Received 19th January 2020,  
Accepted 14th February 2020

DOI: 10.1039/d0qm00040j

rsc.li/frontiers-materials

## Introduction

Atomic site catalysts (ASCs) have been a new frontier of interest in materials and catalytic science due to their distinct advantages in terms of their unique electronic structure and maximum atom utilization.<sup>1–6</sup> However, to keep the metal sites atomically dispersed and avoid agglomeration, the metal loading of ASCs is usually below 1 at%, which leads to low overall activities. Densely populated ASCs are now becoming increasingly important to practical catalysis applications.<sup>7</sup> Recently, our group developed an ion-exchange process to prepare atomic Pt sites embedded in an amorphous CuS<sub>x</sub> support with a concentration as high as 24.8 at%.<sup>8</sup> The strong Pt–S affinity ensured that the Pt would be atomically dispersed on the sulfur-rich support without the formation of Pt clusters. Therefore, a proper support with rich coordination sites (*e.g.* N/O/S) to anchor the metal atoms is the key to ensure the high density atomically dispersed structure.

Metal–organic frameworks (MOFs), assembled by metal nodes and organic ligands, have been intensely investigated as novel porous materials with controlled architectures, abundant anchoring sites and atomic level structure modularity.<sup>9–11</sup> It can be founded that the metal nodes are atomically dispersed in the MOFs naturally possessing a well-defined coordination with the

organic ligands. The cation exchange of the metal nodes is an attractive way to introduce densely distributed atomic metal sites into the MOFs topology.<sup>12,13</sup> For example, the nonprecious 3d transition metals have been widely reported to partially substitute the Zn nodes in the zeolitic imidazolate framework (ZIF-8), and the further derived high-density atomic catalysts have shown excellent performance in many crucial catalytic reactions.<sup>14–19</sup> However, densely populated noble metal atomic catalysts supported in MOFs have been rarely reported.

Hollow nanomaterials have attracted a broad interest due to their unique structures and abundant beneficial physicochemical properties.<sup>20–23</sup> Herein, we report a novel amorphous nanobox (NB) with high-density atomic platinum (A-Pt NB) derived from ZIF-8 nanocubes. The catalytically active noble metal Pt is uniformly dispersed into the MOF skeleton by cation exchange and then the MOF is gradually evolved into a hollow nanostructure through the Kirkendall effect. The dispersing–etching strategy endowed the nanobox with coordination unsaturated atomic platinum at an ultrahigh density which was anchored by N atoms in the distorted MOF skeleton. Such low-coordination atomic platinum exhibits excellent performance in C–H bond activation which could bridge the gap between homogeneous and heterogeneous catalysis.

## Results and discussion

## Synthesis of the A-Pt NBs

The ZIF-8 nanocubes were first synthesized according to the reported method to serve as the precursor for the following dispersing–etching process.<sup>24</sup> Transmission electron microscopy (TEM) images

<sup>a</sup> Department of Chemistry, Tsinghua University, Beijing 100084, China.  
E-mail: cchen@mail.tsinghua.edu.cn, pengqing@mail.tsinghua.edu.cn,  
ydli@mail.tsinghua.edu.cn

<sup>b</sup> College of Chemistry and Materials Science, Anhui Normal University, Wuhu,  
241000, China

† Electronic supplementary information (ESI) available. See DOI: 10.1039/d0qm00040j

‡ These authors contribute equally.

and X-ray diffraction (XRD) patterns show the uniform cube morphology and the well-defined structure of ZIF-8 (Fig. 2a and e).

A dispersing-etching strategy similar to the method we have reported previously is developed to prepare the A-Pt NB.<sup>25</sup> The as-prepared ZIF-8 nanocubes were dispersed in a water and methanol solution. Then,  $K_2PtCl_4$  was introduced into the above solution, and the mixture was uniformly stirred and underwent a solvothermal reaction. During the process, the noble metal  $Pt^{2+}$  is uniformly dispersed into the ZIF-8 skeleton by cation exchange, then the ZIF-8 nanocubes are etched and converted to hollow nanoboxes through the Kirkendall effect.

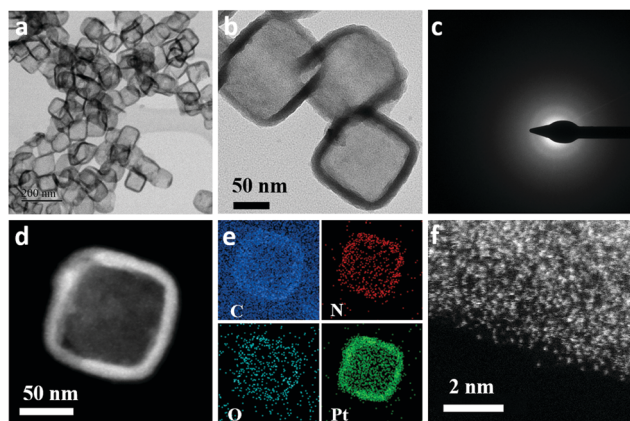


Fig. 1 Structure characterization of A-Pt NBs. (a) The AC-STEM image. (b) The TEM image. (c) The SAED of (d). (d) The HAADF-STEM image. (e) The EDS elemental mapping. (f) The AC HAADF-STEM image.

As shown in the aberration corrected scanning transmission electron microscopy (AC-STEM) and TEM images (Fig. 1a and b), the A-Pt NBs exhibited a hollow nanobox morphology, inheriting the shape of the ZIF-8 nanocubes (Fig. S1, ESI<sup>†</sup>). The high angle annular dark-field scanning transmission electron microscopy (HAADF-STEM) and energy-dispersive X-ray spectroscopy (EDS) elemental mapping images revealed that Pt, N, O and C elements are homogeneously distributed over the entire nanobox (Fig. 1d and e), which indicated a homo-distribution of the Pt species without obvious aggregation. The high resolution TEM (HRTEM) selected area electron diffraction (SAED) image of an individual A-Pt NB presents an amorphous diffraction ring, implying the breaking of the well-defined ZIF-8 topology (Fig. 1c). To verify that it is atomic Pt species on the nanoboxes, we performed aberration corrected HAADF-STEM (AC HAADF-STEM) measurements. As shown in Fig. 1f, high-concentration but randomly distributed, isolated bright dots are observed, which are identified as the atomic Pt species. It is clear that almost all the Pt species exist exclusively at isolated atomic sites; no Pt nanoparticles are detected. Besides, the A-Pt NBs exhibited a high surface area of  $106 \text{ m}^2 \text{ g}^{-1}$  according to the Brunauer-Emmett-Teller (BET) adsorption-desorption isotherms, which can facilitate the diffusion and mass transfer of substrate molecules in the following catalysis process (Fig. S2, ESI<sup>†</sup>). These results suggest that a large number of atomic Pt species were dispersed in the distorted MOF skeleton with a distinct amorphous feature.

#### Structure evolution of the A-Pt NBs

To better understand the formation mechanism of A-Pt NBs, we tracked the entire evolution process by monitoring the intermediates at different stages.

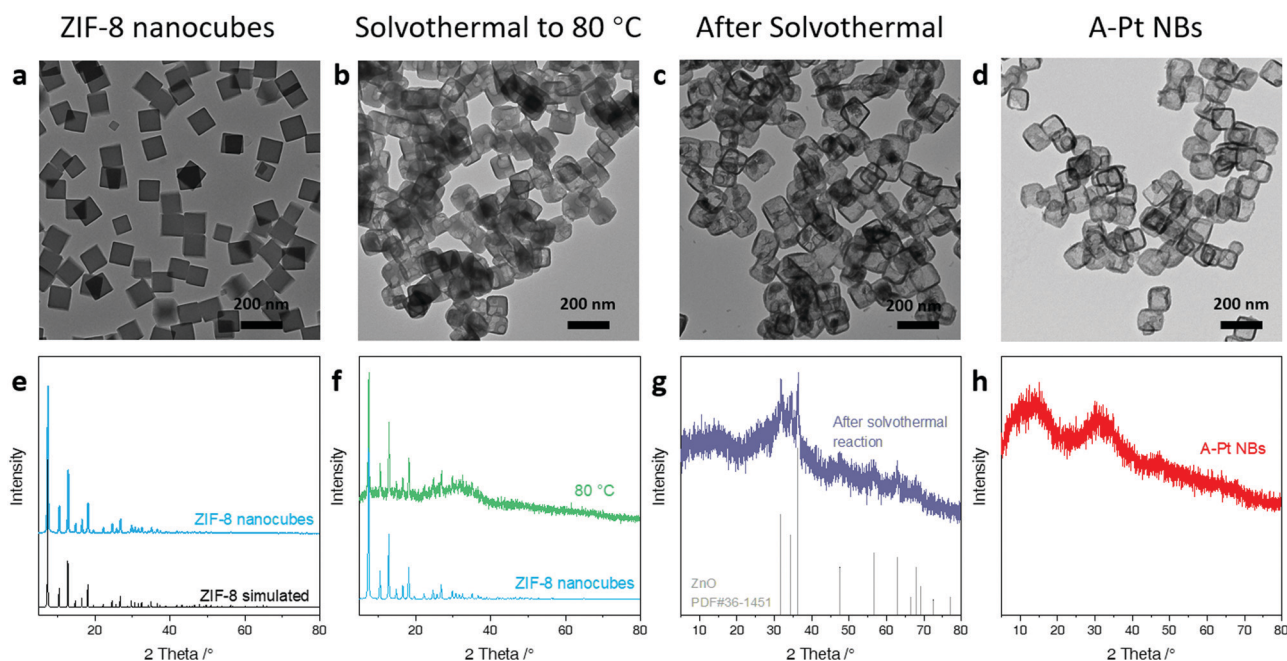


Fig. 2 The TEM images (top row) and XRD patterns (bottom row) of the samples obtained at four representative stages during the structure evolution process of A-Pt NBs. (a) and (e) The initial ZIF-8 nanocubes. (b) and (f) The samples obtained when the solvothermal reaction temperature rise to  $80 \text{ }^\circ\text{C}$ . (c) and (g) The samples obtained after the solvothermal reaction. (d) and (h) The final A-Pt NBs obtained after  $\text{NH}_3\text{H}_2\text{O}$  etching of ZnO.

When the solvothermal reaction started,  $\text{Pt}^{2+}$  gradually replaced  $\text{Zn}^{2+}$  in the skeleton of ZIF-8 *via* cation exchange due to the strong coordination interaction between Pt and N. Due to the diffusion of the  $\text{Zn}^{2+}$  cations out of the shell being faster than the in-diffusion of  $\text{Pt}^{2+}$  cations, a mild phase transition occurred at the same time according to the Kirkendall effect. The continuous consumption of the ZIF-8 core led to the gap between the newly formed shell and the rest of the ZIF-8 core. When the temperature rises to 80 °C, an intermediate part-etched structure can be obtained. The TEM image shows that the initially solid nanocubes began to be eroded and the XRD pattern revealed that the intermediates at this stage still retained the crystalline structure of ZIF-8 (Fig. 2).

The internal ZIF-8 core was gradually dissolved as the solvothermal reaction continues, leaving a stable core-shell structure. The XRD pattern of the samples after solvothermal reaction indicated a hexagonal ZnO phase (JCPDS #36-1451, Fig. 2), which indicates that the redundant  $\text{Zn}^{2+}$  during the phase change process may have undergone hydrolysis and oxidation to form the ZnO core. This dispersion-etching strategy can also be adapted to synthesize other noble-metal hollow structures, such as Au nanoboxes and Pd nanoboxes (Fig. S3, ESI†).

The ZnO core was further removed by the  $\text{NH}_3\text{H}_2\text{O}$  etching, leaving the final hollow nanobox structure with high-density atomic Pt. The poor crystallinity of the A-Pt NBs was evidenced by the broadened XRD pattern which was consistent with the SAED results as discussed above. Such amorphous features may result from the major substitution of  $\text{Zn}^{2+}$  in ZIF-8 by the large numbers of  $\text{Pt}^{2+}$  which breaks the well-defined topology. According to the inductively coupled plasma-optical emission spectrometry (ICP-OES) and X-ray photoelectron spectroscopy (XPS) surface elemental analysis, the Pt content is as high as 6.24 at% (atomic ratio, based on the XPS) or 47 wt% (mass ratio, 46.92 wt% based on the XPS and 47.38 wt% based on the ICP-OES), while the Zn content is only 2 at% (based on the XPS) (Table S1, ESI†). The metal loading can be further confirmed by the thermogravimetric analysis (TGA) (Fig. S4, ESI†). It should be noted that the analogous ZIF consisting of Pt metal and the 2-methylimidazole organic ligand is unavailable through direct synthesis. Therefore, when a large proportion of  $\text{Zn}^{2+}$  in ZIF-8 was substituted by  $\text{Pt}^{2+}$ , the lattice mismatch intensifies, leads to the breaking of the well-defined ZIF topology. As a result, the high-density Pt species were uniformly dispersed and stabilized in the distorted metal-organic skeleton without further aggregation.

### Fine structure characterization of the A-Pt NBs

Further characterizations were conducted to unveil the fine structure of the A-Pt NBs. We performed XPS analysis to obtain insights into the surface structure of the A-Pt NBs (Fig. S5, ESI†). The peaks of the A-Pt NB at 72.5 eV and 75.8 eV are close to the  $\text{Pt(II)} 4f^{7/2}$  and  $4f^{5/2}$ .<sup>26</sup> X-ray absorption spectroscopy (XAS) studies were further carried out to determine the electronic structure and coordination environment of the A-Pt NBs. The white line intensity of the X-ray absorption near-edge structure (XANES) for the Pt  $L_3$ -edge is related to the electronic structure of Pt.<sup>6,8,27</sup> As shown in Fig. 3a, the white line intensity of the

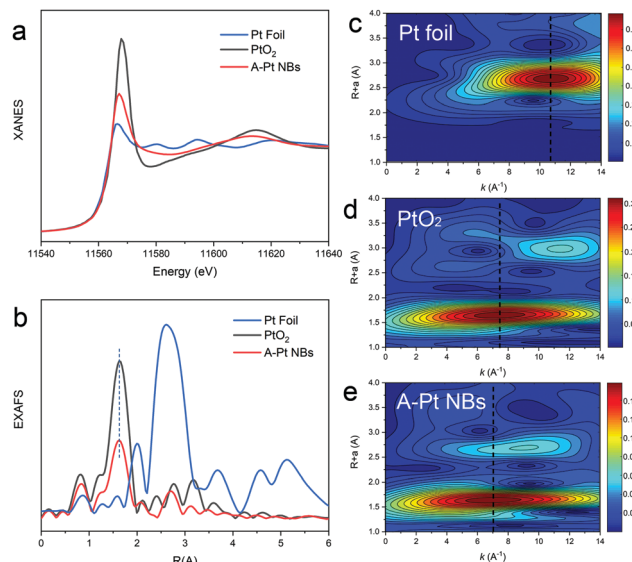


Fig. 3 X-ray absorption spectroscopic studies of the A-Pt NBs. (a) XANES spectra at the Pt  $L_3$ -edge of the A-Pt NBs,  $\text{PtO}_2$ , and Pt foil. (b) Fourier transform (FT) EXAFS spectrum of the A-Pt NBs compared with  $\text{PtO}_2$  and Pt foil at the Pt  $L_3$ -edge. (c–e) Wavelet transform (WT) EXAFS of the Pt foil (c),  $\text{PtO}_2$  (d) and A-Pt NBs (e).

A-Pt NBs is between those of Pt foil and  $\text{PtO}_2$ . A semi-quantitative analysis based on the white line intensity of XANES for the Pt  $L_3$ -edge indicated that the valence of Pt in A-Pt NBs is roughly +1.5, which is consistent with the XPS results (Fig. S6, ESI†).

The coordination environment of Pt in A-Pt NBs is studied using extended X-ray absorption fine structure (EXAFS). The Fourier transform (FT) of the  $k^3$  weighted EXAFS spectra are shown in Fig. 3b. The major peak of the A-Pt NBs at *ca.* 1.6 Å (without phase correction) is close to that of commercial  $\text{PtO}_2$  in the EXAFS, indicating the scattering of Pt and light elements (N/O). Besides the Pt–N bond which could be formed during the cation exchange process, as shown in the Fig. 1e, there are some O atoms around the Pt and N atoms, which indicates that some Pt atoms may coordinate to O atoms under the solvothermal reaction to form possible Pt–O bonds. More importantly, the intensity of the Pt–N/O shell in  $R$  space greatly weakened in comparison to  $\text{PtO}_2$ , which may result from the ratio and the low coordination numbers of Pt–N/O.<sup>16,28</sup> As discussed above, the significant substitution of  $\text{Pt}^{2+}$  for  $\text{Zn}^{2+}$  would break the initial long-range order of ZIF structure and resulted in the distorted skeleton. At the same time, the introduced Pt atoms could not form a well-defined Pt– $\text{N}_4$  coordination structure like Zn– $\text{N}_4$  in the pristine ZIF-8. Instead, a large number of Pt species would coordinate unsaturated due to the dissolution of some organic ligands and the distorted skeleton.

As shown in Fig. 3b, there is a minor peak at around 2.7 Å in the FT-EXAFS of A-Pt NBs that overlaps partially with the Pt–Pt peak (around 2.6 Å) which may result from the backscattering between metal and the next nearest-neighbor light atoms or the metal–metal contributions. To further understand the elemental nature and atomic structure of A-Pt NBs, we performed

wavelet transform (WT) EXAFS analysis which allows a resolution of the backscattering atoms in both  $k$ - and  $R$ -spaces (Fig. 3c–e).<sup>29,30</sup> The WT of  $k^3$ -weighted EXAFS signals clearly reveal a single intensity maximum at around  $10.7 \text{ \AA}^{-1}$  that can be assigned to the Pt–Pt contributions of Pt foil. In marked contrast to the maximum around  $10 \text{ \AA}^{-1}$  resulting from metal–metal contributions, the WT EXAFS showed intensity maximum at about  $7.4 \text{ \AA}^{-1}$  for PtO<sub>2</sub> and about  $7.0 \text{ \AA}^{-1}$  for A–Pt NBs, which can be assigned to the metal–C/N/O contribution of the first nearest-neighbor coordination shell. Therefore, the minor peak at around  $2.7 \text{ \AA}$  in the FT-EXAFS can be assigned to the second shell Pt–C/N/O contributions rather than Pt–Pt contributions. The maximum feature at around  $9.0 \text{ \AA}^{-1}$  in WT-EXAFS might result from the effect of side lobes and the multiple scattering paths between the light atoms. Combined with the FT-EXAFS and WT-EXAFS, we can confirm that the Pt species are atomically dispersed in the nanoboxes without aggregation to nanoparticles.

### Catalytic performance of the A–Pt NBs

Arylboronic acids and their derivatives can be used as intermediates for the conversion of various chemical functional groups, therefore they possess significantly high chemical value.<sup>31–34</sup> Direct C–H borylation without an aromatic halogenated hydrocarbon step is the most attractive way to synthesize arylboronic acid derivatives. However, the catalysts for direct C–H borylation are mostly iridium/platinum complexes in a homogeneous form, which suffer from the recovery and recycling drawbacks.<sup>35</sup> The first shell coordination of the atomic metal sites can play the role of organic modifiers of homogeneous catalysts to some extent, which may modify the metal centers to show analogous homogeneous catalytic performance.<sup>36</sup> Therefore, atomic site catalysts with well-defined metal centers are promising candidates which can serve as a bridge for converting from homogeneous catalysis to heterogeneous catalysis.

Given the high-density atomic Pt and the diffusion advantage of the hollow nanobox structure, we used the A–Pt NBs as a heterocatalyst for the direct C–H bond borylation of toluene with B<sub>2</sub>pin<sub>2</sub> (Fig. 4a). As shown in Fig. 4b, the A–Pt NBs show 99% conversion of B<sub>2</sub>pin<sub>2</sub> in 10 h at 120 °C through a condition optimization and kinetics study, which is superior to the commercial Pt/C catalysts, PtO<sub>2</sub> and Pt salt (Fig. 4c). Unfortunately, it is hard to obtain a good borylation selectivity of all the catalysts. However, the A–Pt NBs shows a robust cycling stability compared with the homogeneous catalysts. The C–H bond borylation activity was well retained after three cycles without any additional re-activation (Fig. S7, ESI†). Meanwhile, the structure stability was confirmed by TEM and XAS studies. The TEM images and XAS of catalysts obtained after three catalytic cycles showed no significant change compared with the initial ones (Fig. S8 and S9, ESI†). Besides, the A–Pt NBs exhibit a high tolerance for a diverse range of arenes with different substituents (Fig. S10, ESI†).

Several factors could contribute to the excellent C–H bond activity of A–Pt NBs: (i) the hollow nanobox structure could facilitate mass transfer and molecular diffusion. (ii) The coordination unsaturated Pt–N/O species behave like the platinum and organic modifiers of the homogeneous catalysts, which may account for the similar activity. (iii) The high-density atomic Pt species provide abundant active centers for the C–H bond borylation and elevate the overall reaction activity.

## Conclusions

In summary, we successfully synthesized A–Pt NBs by cation exchange with the ZIF-8 precursor. Such atomic site catalysts possess ultrahigh noble metal loading which benefits from the dispersing–etching strategy. This work could provide new insights into the design of densely populated atomic site catalysts on metal–organic frameworks or other suitable supports with abundant anchor sites.

## Experimental

### Chemicals and reagents

Analytical grade zinc nitrate hexahydrate (Zn(NO<sub>3</sub>)<sub>2</sub>·6H<sub>2</sub>O), and commercial PtO<sub>2</sub> and Pt/C (5%) catalysts were purchased from Alfa Aesar. 2-Methylimidazole was purchased from Aladdin. Potassium tetrachloroplatinate(II) was purchased from Innocem. All chemicals were from commercial sources and used without further purification.

### Synthesis of ZIF-8 nanocubes

Zn(NO<sub>3</sub>)<sub>2</sub>·6H<sub>2</sub>O (0.3626 g) was dissolved in 12.5 mL deionized water to form solution A. 2-Methylimidazole (5.6752 g) and CTAB (0.0175 g) were dissolved in 87.5 mL of deionized water to form solution B. Then solution A was rapidly injected into the solution B followed by 5 min stirring. The resulting suspension was aged at 28 °C for 3 h to obtain a ZIF-8 nanocubes dispersion.

### Synthesis of A–Pt NBs

8 mL of as-synthesized ZIF-8 nanocubes dispersion was centrifuged and re-dispersed uniformly in 4 mL deionized water by sonication to form dispersion C. K<sub>2</sub>PtCl<sub>4</sub> (0.1 mmol)

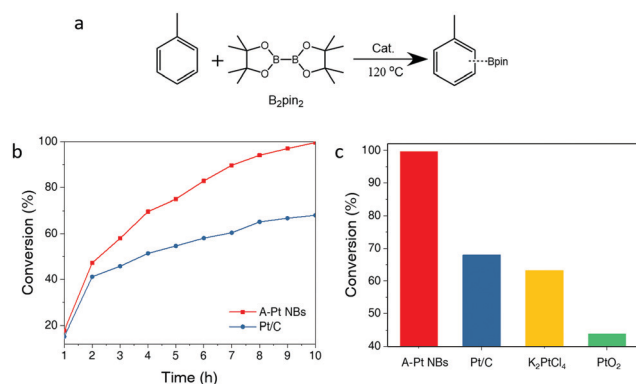


Fig. 4 The catalytic test. (a) Chemical equation for C–H bond borylation of toluene. (b) Kinetics study. (c) Catalytic performance of the C–H bond borylation using different catalysts.

was dissolved in 3 mL deionized water to form solution D. Then, D and 1 mL MeOH were added into C, then the mixture dispersion was heated to 80 °C for 2 h under stirring. The precipitates were obtained by centrifugation and washed with MeOH 3 times and re-dispersed in 4 mL H<sub>2</sub>O then 1 mL NH<sub>3</sub>H<sub>2</sub>O was injected into the dispersion followed by 20 min stirring. The final product A-Pt NBs were obtained by centrifugation and washed with MeOH 3 times and vacuum dried.

### Characterization

TEM images were obtained on a Hitachi-7700 TEM operated at 100 kV. XRD data were measured on a Bruker D8 Advance diffractometer (Cu K $\alpha$ ,  $\lambda = 1.5418 \text{ \AA}$ , operating at 40 kV/40 mA). The HRTEM and the corresponding EDS elemental mapping were carried out on a FEI Tecnai G2 F20 S-Twin HRTEM working at 200 kV. AC HAADF-STEM images were obtained on a Titan Themis 80-300 STEM operated at 300 kV, equipped with a spherical probe aberration corrector. Elemental analysis was detected using a Thermo IRIS Intrepid II ICP-OES. XPS was performed on a ULVAC PHI Quantera microprobe. XAS study of the Pt L3-edge was all collected at the 1W1B station of the Beijing Synchrotron Radiation Facility using a fixed-exit Si(111) double-crystal monochromator operated at 2.5 GeV with a maximum current of 250 mA in transmission mode. Pt foil and PtO<sub>2</sub> were used as references.

### Catalysis testing

Typically, the C–H bond borylation of arenes was carried out in a 10 mL standard Schlenk tube outfitted with a temperature controller and stirrer. 20 mg catalysts and 30 mmol arenes were added to the reactor followed by an hour of sonication. Then B<sub>2</sub>pin<sub>2</sub> (0.25 mmol) was added into the above mixture, and heated to 120 °C and vigorously stirred for 10 h. The conversion was determined by GC-MS and GC analysis with dodecane as the internal standard.

## Conflicts of interest

There are no conflicts to declare.

## Acknowledgements

This work was supported by the National Natural Science Foundation of China (21971135, 21925202, 21872076) and Beijing Natural Science Foundation (JQ18007). This work was supported by Tsinghua University Initiative Scientific Research Program. We thank the 1W1B station for XAFS measurements at the Beijing Synchrotron Radiation Facility (BSRF).

## Notes and references

- J. Gu, C.-S. Hsu, L. Bai, H. M. Chen and X. Hu, Atomically dispersed Fe<sup>3+</sup> sites catalyze efficient CO<sub>2</sub> electroreduction to CO, *Science*, 2019, **364**, 1091–1094.
- J. Jones, H. Xiong, T. A. DeLaRiva, J. E. Peterson, H. Pham, R. S. Challa, G. Qi, S. Oh, H. M. Wiebenga, X. I. P. Hernández, Y. Wang and K. A. Datye, Thermally stable single-atom platinum-on-ceria catalysts *via* atom trapping, *Science*, 2016, **353**, 151–154.
- H. B. Yang, S.-F. Hung, S. Liu, K. Yuan, S. Miao, L. Zhang, X. Huang, H.-Y. Wang, W. Cai, R. Chen, J. Gao, X. Yang, W. Chen, Y. Huang, H. M. Chen, C. M. Li, T. Zhang and B. Liu, Atomically dispersed Ni(I) as the active site for electrochemical CO<sub>2</sub> reduction, *Nat. Energy*, 2018, **3**, 140–147.
- D. Liu, X. Li, S. Chen, H. Yan, C. Wang, C. Wu, Y. A. Haleem, S. Duan, J. Lu, B. Ge, P. M. Ajayan, Y. Luo, J. Jiang and L. Song, Atomically dispersed platinum supported on curved carbon supports for efficient electrocatalytic hydrogen evolution, *Nat. Energy*, 2019, **4**, 512–518.
- L. Cao, W. Liu, Q. Luo, R. Yin, B. Wang, J. Weissenrieder, M. Soldemo, H. Yan, Y. Lin, Z. Sun, C. Ma, W. Zhang, S. Chen, H. Wang, Q. Guan, T. Yao, S. Wei, J. Yang and J. Lu, Atomically dispersed iron hydroxide anchored on Pt for preferential oxidation of CO in H<sub>2</sub>, *Nature*, 2019, **565**, 631–635.
- B. Qiao, A. Wang, X. Yang, L. F. Allard, Z. Jiang, Y. Cui, J. Liu, J. Li and T. Zhang, Single-atom catalysis of CO oxidation using Pt<sub>1</sub>/FeO<sub>x</sub>, *Nat. Chem.*, 2011, **3**, 634–641.
- J. Wu, L. Xiong, B. Zhao, M. Liu and L. Huang, Densely Populated Single Atom Catalysts, *Small Methods*, 2019, 201900540.
- R. Shen, W. Chen, Q. Peng, S. Lu, L. Zheng, X. Cao, Y. Wang, W. Zhu, J. Zhang, Z. Zhuang, C. Chen, D. Wang and Y. Li, High-Concentration Single Atomic Pt Sites on Hollow CuS<sub>x</sub> for Selective O<sub>2</sub> Reduction to H<sub>2</sub>O<sub>2</sub> in Acid Solution, *Chem*, 2019, **5**, 2099–2110.
- G. Li, S. Zhao, Y. Zhang and Z. Tang, Metal–Organic Frameworks Encapsulating Active Nanoparticles as Emerging Composites for Catalysis: Recent Progress and Perspectives, *Adv. Mater.*, 2018, 1800702.
- Y. V. Kaneti, J. Tang, R. R. Salunkhe, X. Jiang, A. Yu, K. C. Wu and Y. Yamauchi, Nanoarchitected Design of Porous Materials and Nanocomposites from Metal–Organic Frameworks, *Adv. Mater.*, 2017, **29**, 1604898.
- S. Pullen, H. Fei, A. Orthaber, S. M. Cohen and S. Ott, Enhanced photochemical hydrogen production by a molecular diiron catalyst incorporated into a metal–organic framework, *J. Am. Chem. Soc.*, 2013, **135**, 16997–17003.
- W. Zhao, G. Li and Z. Tang, Metal–organic frameworks as emerging platform for supporting isolated single-site catalysts, *Nano Today*, 2019, **27**, 178–197.
- Z. Liang, C. Qu, D. Xia, R. Zou and Q. Xu, Atomically dispersed metal sites in MOF-based materials for electrocatalytic and photocatalytic energy conversion, *Angew. Chem., Int. Ed.*, 2018, **57**, 9604–9633.
- C. Zhao, X. Dai, T. Yao, W. Chen, X. Wang, J. Wang, J. Yang, S. Wei, Y. Wu and Y. Li, Ionic Exchange of Metal–Organic Frameworks to Access Single Nickel Sites for Efficient Electroreduction of CO<sub>2</sub>, *J. Am. Chem. Soc.*, 2017, **139**, 8078–8081.

- 15 P. Yin, T. Yao, Y. Wu, L. Zheng, Y. Lin, W. Liu, H. Ju, J. Zhu, X. Hong, Z. Deng, G. Zhou, S. Wei and Y. Li, Single Cobalt Atoms with Precise N-Coordination as Superior Oxygen Reduction Reaction Catalysts, *Angew. Chem., Int. Ed.*, 2016, **55**, 10800–10805.
- 16 X. Wang, Z. Chen, X. Zhao, T. Yao, W. Chen, R. You, C. Zhao, G. Wu, J. Wang, W. Huang, J. Yang, X. Hong, S. Wei, Y. Wu and Y. Li, Regulation of Coordination Number over Single Co Sites: Triggering the Efficient Electroreduction of CO<sub>2</sub>, *Angew. Chem., Int. Ed.*, 2018, **57**, 1944–1948.
- 17 S. Ji, Y. Chen, S. Zhao, W. Chen, L. Shi, Y. Wang, J. Dong, Z. Li, F. Li, C. Chen, Q. Peng, J. Li, D. Wang and Y. Li, Atomically Dispersed Ruthenium Species Inside Metal–Organic Frameworks: Combining the High Activity of Atomic Sites and the Molecular Sieving Effect of MOFs, *Angew. Chem., Int. Ed.*, 2019, **58**, 4271–4275.
- 18 Y. Chen, S. Ji, Y. Wang, J. Dong, W. Chen, Z. Li, R. Shen, L. Zheng, Z. Zhuang, D. Wang and Y. Li, Isolated Single Iron Atoms Anchored on N-Doped Porous Carbon as an Efficient Electrocatalyst for the Oxygen Reduction Reaction, *Angew. Chem., Int. Ed.*, 2017, **56**, 6937–6941.
- 19 H. Fei, J. F. Cahill, K. A. Prather and S. M. Cohen, Tandem postsynthetic metal ion and ligand exchange in zeolitic imidazolate frameworks, *Inorg. Chem.*, 2013, **52**, 4011–4016.
- 20 J. Wang, J. Wan and D. Wang, Hollow Multishelled Structures for Promising Applications: Understanding the Structure-Performance Correlation, *Acc. Chem. Res.*, 2019, **52**, 2169–2178.
- 21 J. Wang, H. Tang, H. Wang, R. Yu and D. Wang, Multi-shelled hollow micro-/nanostructures: promising platforms for lithium-ion batteries, *Mater. Chem. Front.*, 2017, **1**, 414–430.
- 22 J. Wang, H. Tang, L. Zhang, H. Ren, R. Yu, Q. Jin, J. Qi, D. Mao, M. Yang, Y. Wang, P. Liu, Y. Zhang, Y. Wen, L. Gu, G. Ma, Z. Su, Z. Tang, H. Zhao and D. Wang, Multi-shelled metal oxides prepared via an anion-adsorption mechanism for lithium-ion batteries, *Nat. Energy*, 2016, **1**, 16050.
- 23 D. Mao, J. Wan, J. Wang and D. Wang, Sequential Templating Approach: A Groundbreaking Strategy to Create Hollow Multishelled Structures, *Adv. Mater.*, 2019, **31**, e1802874.
- 24 Y. Pan, D. Heryadi, F. Zhou, L. Zhao, G. Lestari, H. Su and Z. Lai, Tuning the crystal morphology and size of zeolitic imidazolate framework-8 in aqueous solution by surfactants, *CrystEngComm*, 2011, **13**, 6937–6940.
- 25 Z. Zhuang, Y. Wang, C.-Q. Xu, S. Liu, C. Chen, Q. Peng, Z. Zhuang, H. Xiao, Y. Pan, S. Lu, R. Yu, W.-C. Cheong, X. Cao, K. Wu, K. Sun, Y. Wang, D. Wang, J. Li and Y. Li, Three-dimensional open nano-netcage electrocatalysts for efficient pH-universal overall water splitting, *Nat. Commun.*, 2019, **10**, 4875.
- 26 C. Chen, Y. Kang, Z. Huo, Z. Zhu, W. Huang, H. L. Xin, J. D. Snyder, D. Li, J. A. Herron, M. Mavrikakis, M. Chi, K. L. More, Y. Li, N. M. Markovic, G. A. Somorjai, P. Yang and V. R. Stamenkovic, Highly Crystalline Multimetallic Nanoframes with Three-Dimensional Electrocatalytic Surfaces, *Science*, 2014, **343**, 1339–1343.
- 27 S. Yang, J. Kim, Y. J. Tak, A. Soon and H. Lee, Single-Atom Catalyst of Platinum Supported on Titanium Nitride for Selective Electrochemical Reactions, *Angew. Chem., Int. Ed.*, 2016, **55**, 2058–2062.
- 28 Y. Pan, Y. Chen, K. Wu, Z. Chen, S. Liu, X. Cao, W. C. Cheong, T. Meng, J. Luo, L. Zheng, C. Liu, D. Wang, Q. Peng, J. Li and C. Chen, Regulating the coordination structure of single-atom Fe-N<sub>x</sub>C<sub>y</sub> catalytic sites for benzene oxidation, *Nat. Commun.*, 2019, **10**, 4290.
- 29 H. Fei, J. Dong, M. J. Arellano-Jimenez, G. Ye, N. Dong Kim, E. L. Samuel, Z. Peng, Z. Zhu, F. Qin, J. Bao, M. J. Yacaman, P. M. Ajayan, D. Chen and J. M. Tour, Atomic cobalt on nitrogen-doped graphene for hydrogen generation, *Nat. Commun.*, 2015, **6**, 8668.
- 30 H. Fei, J. Dong, D. Chen, T. Hu, X. Duan, I. Shakir, Y. Huang and X. Duan, Single atom electrocatalysts supported on graphene or graphene-like carbons, *Chem. Soc. Rev.*, 2019, **48**, 5207–5241.
- 31 J.-Y. Cho, M. K. Tse, D. Holmes, R. E. Maleczka Jr. and M. R. Smith III, Remarkably Selective Iridium Catalysts for the Elaboration of Aromatic C–H Bonds, *Science*, 2002, **295**, 305–308.
- 32 H. Chen, S. Schlecht, T. C. Semple and J. F. Hartwig, Thermal, Catalytic, Regiospecific Functionalization of Alkanes, *Science*, 2000, **287**, 1995–1997.
- 33 T. Furukawa, M. Tobisu and N. Chatani, C–H functionalization at sterically congested positions by the platinum-catalyzed borylation of arenes, *J. Am. Chem. Soc.*, 2015, **137**, 12211–12214.
- 34 J. F. Hartwig, Borylation and Silylation of C–H Bonds: A Platform for Diverse C–H Bond Functionalizations, *Acc. Chem. Res.*, 2012, **45**, 864–873.
- 35 F. Wu, Y. Feng and C. W. Jones, Recyclable Silica-Supported Iridium Bipyridine Catalyst for Aromatic C–H Borylation, *ACS Catal.*, 2014, **4**, 1365–1375.
- 36 C. Zhao, H. Yu, J. Wang, W. Che, Z. Li, T. Yao, W. Yan, M. Chen, J. Yang, S. Wei, Y. Wu and Y. Li, A single palladium site catalyst as a bridge for converting homogeneous to heterogeneous in dimerization of terminal aryl acetylenes, *Mater. Chem. Front.*, 2018, **2**, 1317–1322.